







Article

# Cell Type-Specific In Vitro Gene Expression Profiling of Stem Cell-Derived Neural Models

James A. Gregory <sup>1,\*</sup>, Emily Hoelzli <sup>1</sup>, Rawan Abdelaal <sup>1</sup>, Catherine Braine <sup>2</sup>, Miguel Cuevas <sup>2</sup>, Madeline Halpern <sup>3</sup>, Natalie Barretto <sup>3</sup>, Nadine Schrode <sup>3</sup>, Güney Akbalik <sup>1</sup>, Kristy Kang <sup>1</sup>, Esther Cheng <sup>3</sup>, Kathryn Bowles <sup>4</sup>, Steven Lotz <sup>5</sup>, Susan Goderie <sup>5</sup>, Celeste M. Karch <sup>6</sup>, Sally Temple <sup>5</sup>, Alison Goate <sup>4</sup>, Kristen J. Brennand <sup>3</sup> and Hemali Phatnani <sup>1,2</sup>

<sup>1</sup> Center for Genomics of Neurodegenerative Disease, New York Genome Center, New York, NY 10013, USA; ehoelzli@NYGENOME.ORG (E.H.); rawanjamil@gmail.com (R.A.); gakbalik@NYGENOME.ORG (G.A.); kkang@NYGENOME.ORG (K.K.); hphatnani@nygenome.org (H.P.)

<sup>2</sup> Department of Neurology, Columbia University Medical Center, New York, NY 10068, USA; cbraine@NYGENOME.ORG (C.B.); mcuevas@NYGENOME.ORG (M.C.)

<sup>3</sup> Pamela Sklar Division of Psychiatric Genomics, Department of Genetics and Genomics, Icahn School of Medicine at Mount Sinai, New York, NY 10029, USA; madeline.halpern@icahn.mssm.edu (M.H.); natalie.barretto@icahn.mssm.edu (N.B.); nadine.schrode@mssm.edu (N.S.); esther.cheng@icahn.mssm.edu (E.C.); kristen.brennand@mssm.edu (K.J.B.)

<sup>4</sup> Ronald M. Loeb Center for Alzheimer's Disease, Department of Neuroscience, Icahn School of Medicine at Mount Sinai, New York, NY 10029, USA; kathryn.bowles@mssm.edu (K.B.); alison.goate@mssm.edu (A.G.)

<sup>5</sup> Neural Stem Cell Institute, One Discovery Drive, Rensselaer, NY 12144, USA; stevelotz@neuralsci.org (S.L.); susangoderie@neuralsci.org (S.G.); sallytemple@neuralsci.org (S.T.)

<sup>6</sup> Department of Psychiatry, Washington University in St. Louis, St. Louis, MO 63110, USA; karchc@wustl.edu

\* Correspondence: james.alan.gregory@gmail.com

Received: 11 May 2020; Accepted: 2 June 2020; Published: 5 June 2020



**Abstract:** Genetic and genomic studies of brain disease increasingly demonstrate disease-associated interactions between the cell types of the brain. Increasingly complex and more physiologically relevant human-induced pluripotent stem cell (hiPSC)-based models better explore the molecular mechanisms underlying disease but also challenge our ability to resolve cell type-specific perturbations. Here, we report an extension of the RiboTag system, first developed to achieve cell type-restricted expression of epitope-tagged ribosomal protein (RPL22) in mouse tissue, to a variety of in vitro applications, including immortalized cell lines, primary mouse astrocytes, and hiPSC-derived neurons. RiboTag expression enables depletion of up to 87 percent of off-target RNA in mixed species co-cultures. Nonetheless, depletion efficiency varies across independent experimental replicates, particularly for hiPSC-derived motor neurons. The challenges and potential of implementing RiboTags in complex in vitro cultures are discussed.

**Keywords:** hiPSC; neuron; glia; RiboTag; bacTRAP; genomics; RNA-seq

## 1. Introduction

The many cell types of the brain interact to influence each other's function in health and disease [1]. The growing list of rare and common risk loci associated with brain disease implicates a variety of cell types across disorders, with genetic risk sometimes enriched in cell types previously not thought to be related to disease pathology [2]. Non-neuronal and non-cell autonomous effects on neurons are increasingly recognized to play a critical role across psychiatric and neurodegenerative disease [3]. Human-induced pluripotent stem cell (hiPSC)-based models represent a powerful approach to study the complex etiology of brain disease [4]. Towards this, it is necessary to assemble increasingly

complex in vitro models that better capture neuronal circuitry [5], astrocyte support [6], myelination [7], microglia [8], vasculature [9], and blood-brain-barrier functions [10]. However, interrogating cell type-specific processes within increasingly complex networks, particularly of cell types represented at low abundance, is difficult using conventional approaches.

Complementary physical, biochemical, and computational approaches have been developed to identify cell type-specific transcriptomes. Physical methods for isolating cell type-specific RNA include fluorescence-activated cell sorting (FACS) [11,12], single-cell RNA sequencing (scRNA-seq) [13,14], and laser capture microdissection (LCM) [15–17]. Single-cell suspensions required for FACS and scRNA-seq can be challenging to prepare for highly arborized neural cells. scRNA-seq provides cellular resolution data at low read depth and, despite recent advances [18,19], remains prohibitively expensive for large-scale studies. Low read depth and other technical considerations can bias scRNA-seq studies, with certain cell types or transcripts over-represented or missing in the sequencing libraries generated through these methods [20]. LCM is labor intensive, requires highly specialized equipment, and has similar limitations with respect to transcript diversity [21]. Computational approaches to infer cell type abundance and deconvolve cell type-specific transcriptomes from bulk RNA-seq [22] are improving as scRNA-seq reference datasets become more widely available across cell types [23].

RiboTag [24] and translating ribosome affinity purification (TRAP) [25,26] are similar biochemical approaches that rely on cell type-specific expression of epitope-tagged ribosomal subunits to biochemically enrich mRNA from cell types of interest. RiboTag and TRAP leverage the tight interaction between the ribosome and mRNA to indirectly immunoprecipitate (IP) translated RNA via RPL22 or RPL10a, respectively. They do not require specialized equipment, dissociation to single cells, and these methods have been used extensively for studies of murine neurons [27,28], microglia [29], astrocytes [30], and macrophages [31]. We reasoned that the same strategy could be used to purify cell type-specific mRNA from heterogeneous in vitro co-cultures. Additionally, mRNA from multiple cell types could be simultaneously isolated if each cell type expressed a ribosomal subunit with a different epitope tag.

Here, we tested RPL22-fused to V5 [32], hemagglutinin (HA) [33], or Flag [34] affinity tags to IP cell type-specific mRNA; unexpectedly, only RPL22-HA and RPL22-V5 RiboTags co-IPed mRNA. We demonstrate that RPL22-HA and RPL22-V5 IP efficiently enriched mRNA from mixed species co-cultures of immortalized cell lines. When expressed in hiPSC-derived motor neurons (MNs), neural progenitor cells (NPCs), and induced GABAergic neurons (iGANs), IPed RNA was enriched for protein coding genes with a concomitant decrease in lncRNA and mitochondrially encoded genes. Unfortunately, across independent experimental replicates, cell type-specific mRNA enrichment was highly variable in heterocellular cultures composed of hiPSC-derived neurons and primary mouse astrocytes.

## 2. Materials and Methods

### 2.1. Plasmid Construction

All primers and plasmids used in this study are listed in Tables S1 and S2, respectively, and plasmids will be made available at Addgene (Watertown, MA, USA). Oligos were purchased from Integrated DNA Technologies (IDT; Coralville, IA, USA). All plasmids were verified by Sanger sequencing.  $P_{Efla}$ -RPL22-3 $\times$ HA- $P_{2A}$ -EGFP- $T_{2A}$ -Puro was made by Gibson assembly of PCR-amplified cPPT/CTS-EF1a (primers JG101/128; Addgene #52962 template) and RPL22-3 $\times$ HA (primers JG106/109; human cDNA template) with EcoRI/PstI digested pLV-TetO-hNGN2- $P_{2A}$ -eGFP- $T_{2A}$ -Puro (Addgene #79823) backbone.  $P_{Efla}$ -RPL22-3 $\times$ Flag- $P_{2A}$ -EGFP- $T_{2A}$ -Puro was made by ligating PCR-amplified RPL22-3 $\times$ Flag (primers JG131/132) with EcoRI/AgeI-digested  $P_{Efla}$ -RPL22-3 $\times$ HA- $P_{2A}$ -EGFP- $T_{2A}$ -Puro.  $P_{Efla}$ -RPL22-3 $\times$ HA- $P_{2A}$ -EGFP- $T_{2A}$ -Neo was generated by Gibson assembly of RPL22-3 $\times$ HA- $P_{2A}$ -EGFP (primers JG140/141; RPL22-3 $\times$ HA- $P_{2A}$ -EGFP- $T_{2A}$ -Puro template) and NotI/XbaI-digested pLV-TetO-hNGN2- $P_{2A}$ -eGFP- $T_{2A}$ -Neo. To make  $P_{Efla}$ -RPL22-3 $\times$ HA- $P_{2A}$ -mCherry- $T_{2A}$ -Puro,

$P_{Efla}$ -RPL22-3 $\times$ HA- $P_{2A}$ -mCherry- $T_{2A}$ -Neo, and  $P_{Efla}$ -RPL22-3 $\times$ Flag- $P_{2A}$ -mCherry- $T_{2A}$ -Puro, mCherry was first amplified from Addgene plasmid #22418 (primers JG161/162) and cloned into Zero Blunt TOPO (Thermo Fisher Scientific, Waltham, MA, USA). The resulting plasmid was digested with XbaI, and the mCherry fragment was ligated to XbaI-digested  $P_{Efla}$ -RPL22-3 $\times$ HA- $P_{2A}$ -EGFP- $T_{2A}$ -Puro,  $P_{Efla}$ -RPL22-3 $\times$ HA- $P_{2A}$ -EGFP- $T_{2A}$ -Neo, or  $P_{Efla}$ -RPL22-3 $\times$ Flag- $P_{2A}$ -EGFP- $T_{2A}$ -Puro. The 2A peptide sequence causes the ribosome to skip at the 3' end. Thus, an additional short peptide sequence was added to the end of the epitope tag. To test whether the additional amino acids disrupt the normal function of RPL22, we made  $P_{Efla}$ -EGFP- $T_{2A}$ -RPL22-1 $\times$ Flag by Gibson assembly of RPL22-1 $\times$ -Flag (primers JG278/279; RPL22-3 $\times$ HA- $P_{2A}$ -EGFP- $T_{2A}$ -Puro template), EGFP- $T_{2A}$ - (primers JG276/277;  $P_{Efla}$ -RPL22-3 $\times$ HA- $P_{2A}$ -mCherry- $T_{2A}$ -Puro template) and EcoRI/AgeI-digested Addgene #52962.  $P_{Efla}$ -mCherry- $T_{2A}$ -RPL22-1 $\times$ V5 was made by Gibson assembly of RPL22-1 $\times$ V5 (primers JG278/280; RPL22-3 $\times$ HA- $P_{2A}$ -EGFP- $T_{2A}$ -Puro template), mCherry- $T_{2A}$  (primers 277/281;  $P_{Efla}$ -RPL22-3 $\times$ HA- $P_{2A}$ -mCherry- $T_{2A}$ -Puro template), and EcoRI/AgeI-digested Addgene plasmid #52962. To tightly control expression of epitope-tagged RPL22,  $P_{TRE}$ -mCherry- $T_{2A}$ -RPL22-1 $\times$ V5 was generated by Gibson assembly of PCR-amplified mCherry- $T_{2A}$ -RPL22-1 $\times$ V5 (primers JG284/285; template  $P_{Efla}$ -mCherry- $T_{2A}$ -RPL22-1 $\times$ V5) and EcoRI/NheI-digested pLV-TetO-hNGN2- $P_{2A}$ -eGFP- $T_{2A}$ -Puro (Addgene #79823).  $P_{TRE}$ -EGFP- $T_{2A}$ -RPL22-3 $\times$ HA was made by Gibson assembly of GFP- $T_{2A}$  (primers JG290/291;  $P_{Efla}$ -EGFP- $T_{2A}$ -RPL22-1 $\times$ Flag template), RPL22-3 $\times$ HA (JG292/293; RPL22-3 $\times$ HA- $P_{2A}$ -EGFP- $T_{2A}$ -Puro template), and EcoRI/NheI-digested pLV-TetO-hNGN2- $P_{2A}$ -eGFP- $T_{2A}$ -Puro (Addgene #79823). To make Lenti-DIO- $P_{Efla}$ -RPL22-3 $\times$ HA-IRES-YFP, the double-floxed inverse open reading frame (DIO) fragment was amplified from pAAV-Ef1a-DIO-eYFP (gift from Stan McKnight; primers JG303/304) and digested with SpeI.  $P_{Efla}$ -RPL22-3 $\times$ Flag- $P_{2A}$ -EGFP- $T_{2A}$ -Puro was digested with NheI and treated with alkaline phosphatase (AP). The resulting fragments were joined by ligation. Lenti-DIO- $P_{Efla}$ -mCherry- $T_{2A}$ -RPL22-1 $\times$ V5 was made by ligation of PCR-amplified mCherry- $T_{2A}$ -RPL22-1 $\times$ V5 (primers JG284/285; template  $P_{TetR}$ -mCherry- $T_{2A}$ -RPL22-1 $\times$ V5) to AscI/NheI-digested and AP-treated Lenti-DIO- $P_{Efla}$ -RPL22-3 $\times$ HA-IRES-YFP.

## 2.2. Passaging and Maintenance of Cell Lines

HEK293 and 3T3 cells were maintained in Dulbecco's modified Eagle's medium (DMEM) (Thermo Fisher Scientific) supplemented with 10% Cosmic Calf Serum (Thomas Scientific, Swedesboro, NJ, USA) and Antibiotic-Antimycotic (Thermo Fisher Scientific). Feeder-free hiPSCs were maintained on Matrigel (Corning, Corning, NY, USA) or Geltrex (Thermo Fisher Scientific)-coated plates in StemFlex (Thermo Fisher Scientific) as indicated and split either with Accutase (STEMCELL Technologies, Cambridge, MA, USA) or ReleSR (STEMCELL Technologies) as recommended by the manufacturer. hiPSC lines used in this study were generated previously [35] by Sendai viral reprogramming [36]. NPCs were cultured in Dulbecco's modified Eagle's medium: nutrient mixture F-12 (DMEM/F12) supplemented with N2 (Thermo Fisher Scientific), B-27 minus vitamin A (Thermo Fisher Scientific), and fibroblast growth factor-2 (FGF-2) (R&D Systems, Minneapolis, MN, USA) on Matrigel-coated plates as described [37].

## 2.3. Transfections and Lentivirus Production

Plasmids encoding RiboTag constructs were used to transiently transfect HEK293 cells with Lipofectamine 3000 (Thermo Fisher Scientific) as recommended by the manufacturer. Third-generation lentiviruses were produced by polyethylenimine transfection with pCMV-VSV-G (Addgene #8454), pMDLg/pRRE (Addgene #12251), and pRSV-Rev (Addgene #12253) and the appropriate transfer plasmid using established methods [38]. Lentivirus was concentrated by centrifugation, aliquoted, and stored at  $-80^{\circ}\text{C}$ . Prior to use, aliquots of lentivirus were thawed in a water bath at  $37^{\circ}\text{C}$  and added to the appropriate medium.

#### 2.4. FACS

HEK293 cells were dissociated with TrypLE (Thermo Fisher Scientific), washed, resuspended in phosphate-buffered saline (PBS), and filtered through a 40 µm filter. hiPSCs were dissociated using Accutase (STEMCELL technologies), washed, resuspended in PBS containing 1% (*v/v*) bovine serum albumin (BSA), and filtered through a 40 µm filter. Cells positive for mCherry or green fluorescent protein (GFP) were isolated by FACS on a SONY SH800. hiPSCs were plated on Geltrex (Thermo Fisher Scientific) or Matrigel (Corning)-coated plates in StemFlex supplemented with Thiazovivin (Calbiochem, San Diego, CA, USA) for 24 h.

#### 2.5. Neuron Induction and Differentiation

hiPSCs were differentiated into MNs according to Maury et al. [39]. Briefly, embryoid bodies (EBs) were made by dissociating hiPSCs with Accutase and seeding onto low attachment plates (Corning) in supplemented N2B27. Neural induction occurs via dual-SMAD inhibition [40] with SB431542 (Stemgent, Beltsville, MD, USA) and LDN-193189 (Stemgent) followed by motor neuron specification by activation of Wnt (Chir-99021; Selleck Chemicals, Houston, TX, USA), retinoic acid (RA; Sigma Aldrich, St. Louis, MO, USA), and hedgehog (HH) (SAG; Millipore Sigma, Burlington, MA, USA) signaling. Neuronal maturation occurs in the continued presence of RA and HH cues, but with the addition of DAPT (Tocris, Bristol, UK), a Notch signaling inhibitor, and glial cell-derived neurotrophic factor (GDNF) and brain-derived neurotrophic factor (BDNF) to increase neuron survival. EBs were dissociated with 0.25% Trypsin (Thermo Fisher Scientific) in the presence of DNase at 37 °C using a thermomixer (Eppendorf, Hauppauge, NY, USA) and plated on Geltrex or Matrigel-coated plates. Lentivirus encoding RiboTag constructs was added when plating dissociated EBs or to plated neurons for twenty-four hours.

Induced excitatory neurons were produced by overexpression of NGN2 as described [37]. Briefly, NPCs were seeded onto laminin-coated plates and transduced by spinfection [41] with CMV-*rtTA* (Addgene #19780) and TetO-NGN2-P2A-*Puro* (Addgene #79049). Where indicated, RiboTag lentivirus was added concurrently. NGN2 and RiboTag were induced with 1 µg/mL doxycycline, and transduced cells were selected with 1 µg/mL puromycin. When needed, media were supplemented with cytosine β-*D*-arabinofuranoside (Ara-C; Millipore Sigma) to remove proliferative cells. To avoid RiboTag gene silencing in long-term NGN2-induced neurons, we constructed a lentiviral vector for constitutive expression of NGN2 ( $P_{Efla}$ -NGN2-T2A-NeoR) that can be used in combination with tetracycline-inducible RiboTag vectors.

Induced GABAergic neurons were produced from NPCs by overexpression of *Ascl1* and *Dlx2* [42,43]. NPCs were transduced by spinfection with lentivirus encoding CMV-*rtTA* (Addgene #19780), TetO-*Ascl1*-T2A-*Puro* (Addgene #97329), TetO-*Dlx2*-IRES-*Hygro* (Addgene #97330), and the indicated RiboTag construct. Doxycycline was added for fourteen days starting 24 h post-transduction. Transduced cells were selected for five days with puromycin and hygromycin starting 48 h post-transduction. Cells were switched to neuronal medium (Neurobasal (ThermoFisher, #21103049) supplemented with Anti-Anti (ThermoFisher, #15240062), N2 (ThermoFisher, 17502-048), B-27 minus vitamin A (ThermoFisher, #12587-010), GlutaMAX (ThermoFisher, #35050061), 1 mg/mL natural mouse laminin (ThermoFisher, #23017-015), 20 ng/mL BDNF (Peprotech, #450-02, Rocky Hill, NJ, USA), 20 ng/mL GDNF (Peprotech, #450-10), 500 µg/mL cyclic adenosine monophosphate (cAMP) (Sigma, D0627), and 200 nM L-ascorbic acid (Sigma, #A0278) on day seven. Half medium changes were performed every second day.

#### 2.6. Primary Mouse Astrocytes

Primary mouse mixed glia cultures were derived from P0 or P1 B6.SJL animals as previously described [44]. Briefly, cortices were dissected, and meninges were removed. Tissue was digested in 0.25% Trypsin with ethylenediaminetetraacetic acid (EDTA) followed by trituration and then strained



through a 100 µm strainer. Cells were resuspended in 5 mL of Cortex Glial Medium (10% FBS, 1% Pen/Strep, in High Glucose DMEM with Sodium Pyruvate) and plated in T25s coated with 20 µg/mL of Poly-L-Ornithine.

### 2.7. hiPSC-MN and Primary Mouse Astrocyte Co-Cultures

RiboTag-transduced primary astrocytes were resuspended in motor neuron medium supplemented with 2% FBS and added to three- to four-week-old hiPSC-MNs that were previously transduced with a compatible RiboTag construct. hiPSC-MNs and primary mouse astrocytes were co-cultured for at least one week prior to IP.

### 2.8. Cortical-Enriched Organoid and Microglia Co-Cultures

Human cortical-enriched organoids (hCO) were made based on the protocol in [45]. Human iPSC lines obtained from the Tau Consortium cell line collection ([www.http://neuralsci.org/tau](http://neuralsci.org/tau)) (GIH7-C2Δ2B12 (MAPT V337V CRISPR corrected to WT/WT), GIH7-C2Δ2A01 (MAPT V337M/WT), and ND32951A.15Δ1B06 (MAPT V337V Crispr corrected to WT/WT), NeuraCell [46], Rennselaer NY, USA) were maintained in mTeSRTM1 medium (STEMCELL Technologies, catalog #05851) based on feeder-free culture protocols in six-well plates (Corning, catalog #3506) coated with growth factor-reduced Matrigel (Corning, catalog #356231). At 80–85% confluency, hiPSC colonies were lifted with Accutase (Innovative Cell Technologies, #NC9839010, San Diego, CA, USA), a single cell suspension was created, and cells were resuspended in E8 medium with rho-associated, coiled-coil-containing protein kinase 1 (ROCK) inhibitor, Y-27632 (Tocris, catalog #1254), at 2 million cells/mL. Then, 3 million cells were added per well in an AggreWell™800 plate (STEMCELL Technologies, catalog #34811) (10,000 cells per microwell) and incubated for one day. The resulting spheroids were removed from the microwells and transferred to low-attachment dishes in E6 medium supplemented with 2.5 µM Dorsomorphin (DM) (Tocris, catalog #3093), 10 µM SB431542 (Tocris, catalog #1614), and 2.5 µM XAV-939 (Tocris #3748) to initiate neural differentiation through dual-SMAD inhibition [40]. On day 6, the medium was changed to Neurobasal-A (Life Technologies, #10888-022, Carlsbad, CA, USA) plus B-27 supplement without vitamin A (Life Technologies, catalog #12587010), GlutaMax (Life Technologies, #3505-061), Antimycotic (Life Technologies, #15240-062), 20 ng/mL FGF2 (R&D Systems, #233-FB), and 20 ng/mL epidermal growth factor (EGF) (Peprotech, # AF-100-15). On day 25, FGF2 and EGF were replaced with 20 ng/mL BDNF (Peprotech, # 450-02) plus 20 ng/mL Neurotrophin-3 (NT3) (Peprotech, # 450-03). From day 43 onwards, the medium was changed every four days using only the prior medium without growth factors. On day 20, organoids were QCed by fixing overnight at 4 °C in 4% paraformaldehyde (Santa Cruz, Dallas, TX, USA) followed by sucrose cryoprotection, embedding in optimal cutting temperature (OCT) compound, and cryosectioning at 20 µm thickness, then staining for PAX6 (Biolegend, #901301, 1:200, San Diego, CA, USA), SOX2 (Santa Cruz, #sc-365823, 1:100), and B-tubulin III (Sigma, # T-8660, 1:1000).

For GIH7-C2-2A01, ND32951A.15-B06, and GIH7-C2-2B12 hCO co-cultures, approximately 500,000 human microglia (HMC3, ATCC CRL-3304, Manassas, VA, USA) transduced with a RiboTag construct were added to 10-month-old hCOs in 6-well low-attachment plates. hCOs and microglia were co-cultured for three weeks prior to immunoprecipitation. Then, 1, 3, or 6 hCOs were pooled for immunoprecipitation. Doxycycline was added one day prior to immunoprecipitation.

### 2.9. Epitope-tagged RPL22 Immunoprecipitation

Cycloheximide (CHX) is a translational inhibitor that blocks elongation by inhibiting eEF2-mediated translocation [47]. The tight interaction between the ribosome and mRNA in the presence of CHX allows mRNA to be indirectly purified by IP of epitope-tagged RPL22. A detailed protocol can be found in the supplementary methods. Briefly, cells were washed with PBS and resuspended in ice-cold polysome buffer (50 mM Tris-HCl pH 7.4, 100 mM KCl, 5 mM MgCl<sub>2</sub>, 1 mM dithiothreitol (DTT)) supplemented with CHX (100 µg/mL; Sigma–Aldrich), Turbo DNase (20 U/mL;

Thermo Fisher Scientific), Superase-In (400 U/mL; Thermo Fisher Scientific), and protease inhibitor cocktail (Sigma–Aldrich; cat# P8340). Cells were lysed on ice by the addition of NP-40 (1% *v/v* final concentration) and sodium deoxycholate (0.5% *v/v* final concentration), cleared by centrifugation, and filtered using a 100 kDa Amicon ultra-2 filter unit (Millipore Sigma). Aliquots were removed for input control RNA and Western blot analysis. Anti-HA (Thermo Fisher Scientific) or anti-V5 (MBL International, Woburn, MA, USA) magnetic beads were washed with polysome buffer supplemented with Tween (0.1% *v/v* final concentration), added to the lysate, and incubated for at least 4 h at 4 °C using end-over-end mixing. Beads were washed with high-salt polysome buffer (50 mM Tris-HCl pH 7.4, 300 mM KCl, 5 mM MgCl<sub>2</sub>) supplemented with NP-40 (0.5% *v/v* final concentration), CHX (100 µg/mL), Superase-In (20 U/mL), and protease inhibitor. For sequential immunoprecipitations, the supernatant was kept and used for an additional immunoprecipitation with the appropriate antibody. For Western blot analysis, beads were resuspended in Laemmli Sample buffer (Bio-Rad Laboratories, Hercules, CA) supplemented with β-mercaptoethanol (BME) and boiled at 95 °C for 5 min. For RNA purification, beads were resuspended in Trizol, incubated at room temperature for 3 min, and stored at –80 °C.

### 2.10. Western Blot

Cell lysates were made as indicated, prepared with Laemmli sample buffer supplemented with BME, and boiled prior to sodium dodecyl sulfate polyacrylamide gel electrophoresis (SDS-PAGE). Samples were resolved using 4–20% Mini-PROTEAN TGX precast protein gels (Bio-Rad Laboratories), transferred to nitrocellulose, blocked with 5% milk in Tris buffered Saline (TBS; 50 mM Tris, 150 mM NaCl) with 0.1% Tween-20 (TBS-T). Primary antibodies include alkaline phosphatase-conjugated anti-Flag (Sigma–Aldrich A9469) and anti-HA antibodies (ImmunoReagents #MuxOt-111-DALP, Raleigh, NC, USA), biotin-conjugated anti-HA (Biolegend 901505) and anti-V5 (Invitrogen MA5-15253-BTIN) antibodies, and unconjugated anti-GFP (Origene TA150070, Rockville, MD, USA), anti-mCherry (Novus NBP2-25158, Centennial, CO, USA). Secondary antibodies used include IRDye680-conjugated anti-rabbit (Li-COR 925-68071, Lincoln, NE, USA) and anti-mouse (Li-COR 926-68020) antibodies, and IRDye800-conjugated anti-rabbit (Li-COR 926-32211), anti-mouse (Li-COR 926-32210), anti-chicken (Li-COR 925-32218), and anti-goat (Li-COR 925-32214). Blots probed with alkaline phosphatase-conjugated antibodies were visualized using nitroblue tetrazolium (NBT) and 5-bromo-4-chloro-3-indolyl phosphate (BCIP) in alkaline phosphatase buffer (100mM Tris-HCl pH 9.5, 5 mM MgCl<sub>2</sub>, 100 mM NaCl). IRDye probed blots were visualized using the Li-COR Odyssey CLx.

### 2.11. RNA Extraction

RNA isolated from lysates prior to immunoprecipitation, referred to as input control RNA, was purified using Trizol LS followed by RNeasy Micro Kit (Qiagen, Hilden, Germany) column purification as follows: 100 µL of lysate was combined with 150 µL of RNase free water and 750 µL of Trizol LS. Immunoprecipitated RNA was eluted from antibody-conjugated beads using Trizol. Samples were then extracted with chloroform, centrifuged, and the aqueous phase from the input control and IP RNA was mixed with 500 µL and 200 µL of 70% ethanol, respectively, and applied to RNeasy MinElute columns (Qiagen). Wash and elution steps were carried out according to manufacturer recommendations. RNA concentration was determined using the Qubit 3.0 fluorometer (Thermo Fisher Scientific). RNA quality was assessed by Bioanalyzer (Agilent, Santa Clara, CA, USA).

### 2.12. Reverse Transcription Digital PCR (RT-dPCR)

Reverse transcription digital PCR (RT-dPCR) was carried out using a Formulatrix (Bedford, MA, USA) Constellation digital PCR system using a reaction volume of 12 µL in a 96-well format. Applied Biosystems (Waltham, MA, USA) TaqPath One-Step RT-qPCR Master Mix CG was used for all reactions. All reactions were supplemented with 0.1% (*v/v*) Tween-20. Primers and probes were used at 400 nM and 250 nM, respectively, for detection of *GFP* and *mCherry*. ACTB primers and probes (IDT reference

gene assay - Hs.PT.39a.22214847), were used at 1.5 mM and 750 nM, respectively. Primer and probe sequences are listed in Table S1. Data analysis was performed using R.

### 2.13. RNA Sequencing

RNA was reverse transcribed and amplified using a switching mechanism at the 5' end of the RNA template [13] reaction with Maxima reverse transcriptase (Thermo Fisher Scientific) and the oligonucleotides listed in Table S1. cDNA yield was measured with a Qubit 3.0 Fluorometer, and size distribution was measured by Bioanalyzer (Agilent). Sequencing libraries were constructed using the Nextera DNA Flex kit according to manufacturer instructions (Illumina, San Diego, CA, USA). Libraries were quantified by Qubit Fluorometer and qPCR (size distribution was measured by Bioanalyzer) and sequenced using Illumina MiSeq or NovaSeq.

### 2.14. RNA-Seq Analysis

RNA-seq reads were processed with TrimGalore (v0.4.4) [48] and aligned with STAR (v2.5.2a) [49]. For co-cultures composed of human and mouse cells, reads were aligned to a hybrid reference genome that included the canonical chromosomes from hg38 (1-22,X,Y,MT) and mm20 (1-19,X,Y,MT) and sequences for GFP and mCherry. Reads from RNA-seq from cultures composed of human cells only were aligned to hg38. At the chromosome level, uniquely mapping reads were quantified with samtools (v1.7). At the gene level, uniquely mapping reads were quantified with featureCounts from the Subread package (v1.5.2) [50]. Count matrices were analyzed in R (v3.6). DESeq2 [51] was used for differential expression analysis. Gene set enrichment analysis (GSEA) was carried out using fgsea [52] with ensembl gene biotype annotations. GSEA for chromosome enrichment was carried out using protein coding genes across the canonical chromosomes.

We calculated the depletion efficiency for each IP as follows. For each library, we quantified the number of unique reads mapped to each chromosome and calculated the percentage of the total library represented by each chromosome. We evaluated the relative enrichment for each chromosome compared to the co-culture by plotting the initial percent unique reads (co-culture) against the change in unique reads in the matched IP (IP—coculture). The depletion efficiency for each IP was defined as the negative slope of the regression line for off-target chromosomes (e.g., mouse chromosomes in a human specific IP and vice versa). The upper limit for depletion efficiency is therefore 1 and would occur if the pre-IP proportion of reads for each off-target chromosome is equal to the change in proportion after IP for each of those chromosomes. For example, if 5% of reads from a co-culture mapped to an off-target chromosome and all reads to that chromosome were depleted after IP, the change would also be 5%. If this holds true for all off-target chromosomes, the regression line would have a slope of  $-1$ .

## 3. Results

### 3.1. Construction of Epitope-Tagged RPL22

C-terminal HA-tagged RPL22 has been extensively used to purify cell type-specific RNA from mouse central nervous system (CNS) tissue [24]. We reasoned that RPL22 may tolerate additional epitope tags and, when used in combination, could be used to biochemically separate RNA from multiple cell types in a mixed co-culture if each cell type expresses a uniquely tagged RPL22. We fused RPL22 to three well-established epitope tags (V5, Flag, HA) and cloned them into multicistronic lentiviral vectors with antibiotic resistance genes and/or fluorescent proteins (FPs) separated by picornavirus 2A peptides (Figure S1). All three C-terminal RPL22 fusions (hereafter referred to as RiboTags) accumulated in HEK293 cells when transcription was controlled by the EF1- $\alpha$  promoter (Figure 1A–C—top panels). RPL22-1xV5 (hereafter RPL22-V5), RPL22-1xFlag, and RPL22-3xHA (hereafter RPL22-HA) migrated slightly above the predicted molecular weights of 16.6, 16.1, and 20.5 kDa, respectively. RNA was consistently recovered following immunoprecipitation (IP) of RPL22-HA or RPL22-V5. Conversely,

RNA yields following RPL22-1xFlag or RPL22-3xFlag IP were inconsistent, resulting in minimal to no mRNA recovery. Lack of mRNA recovery, despite RPL22-Flag protein accumulation, suggests that the Flag and 3xFlag epitopes may interfere with incorporation of RPL22 into the ribosome. Consistent with this hypothesis, RPLP0 co-immunoprecipitated with RPL22-HA and RPL22-V5, but not RPL22-Flag (Figure 1A–C—bottom panels) or RPL22-3xFlag (data not shown).

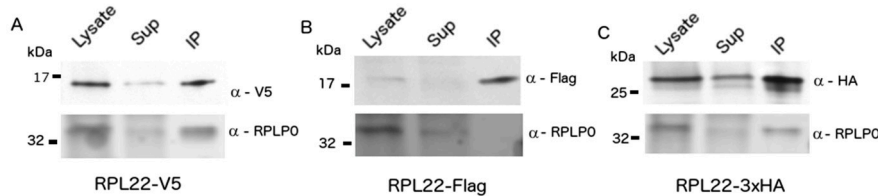


**Figure 1.** RiboTag immunoblot of HEK293 cells expressing RiboTag constructs. HEK293 cells were transduced with lentivirus encoding (A) RPL22-V5, (B) RPL22-Flag, or (C) RPL22-3xHA. Lysates, supernatant (Sup), and immunoprecipitations (IP) were resolved by SDS-PAGE, transferred to nitrocellulose, and detected with antibodies to RPLP0 and V5, Flag, or haemagglutinin (HA).

### 3.2. Biochemical Separation of Cell Type-Specific RNA in Co-Cultures Using RiboTags

To tightly control RiboTag expression, we constructed lentiviral vectors encoding mCherry-T2A-RPL22-V5 and GFP-T2A-RPL22-HA driven by the tetracycline response element ( $P_{TRE}$ ). Additionally, we moved RPL22 to the 3' end of the multicistronic construct to eliminate extra amino acids in the epitope tag resulting from cleavage of the 2A peptide (Figure S2). When used in combination with reverse tetracycline-controlled transactivator (rtTa), RiboTag expression was induced with doxycycline. We generated stable RiboTag HEK293 cell lines via lentiviral transduction and doxycycline induction, followed by FACS. The RPL22-HA and RPL22-V5 expressing cell lines were seeded together in approximately equal numbers. The mixed co-culture was split in half twenty-four hours post-doxycycline induction; half was used for HA IP and the other for V5 IP. GFP and mCherry accumulation were confirmed by microscopy and Western blot (Figure S3A,B). RPL22-HA and RPL22-V5 protein accumulation was confirmed by Western blot using anti-HA and anti-V5 antibodies, respectively (Figure 2A). RPL22-HA appeared as a doublet following IP, suggesting possible degradation. Absolute *GFP* and *mCherry* mRNA abundance was measured by reverse transcription digital PCR (RT-dPCR; Table S3, Figure 2B). Each cell expressed *GFP* or *mCherry*, allowing relative levels to be used as a proxy for cell type-specific mRNA abundance. The initial *mCherry*/*GFP* ratio in mRNA isolated from the co-culture was approximately 9:2 (Figure 2B—yellow). As expected, this ratio increased in mRNA isolated with V5 antibodies and decreased in mRNA isolated with HA antibodies (Table S4; Figure 2B). The combined effect was an 88-fold difference in the *mCherry*/*GFP* ratio between the HA and V5 IP RNA samples.

In the above experiments, co-culture lysates were split equally for HA IP and V5 IP. This strategy reduces the potential RNA yield by half, which is problematic for precious samples or when obtaining large numbers of cells is impractical. We reasoned that immunoprecipitation with HA and V5 antibodies from the same sample could improve RNA recovery. To test this hypothesis, we implemented two strategies. First, we simultaneously immunoprecipitated RPL22-HA and RPL22-V5 using antibody-conjugated magnetic beads followed by sequential elution with HA then V5 peptides or vice versa. We observed incomplete elution of RPL22-V5 using V5 peptides and RPL22-V5 contamination in the HA peptide-eluted fraction (Figure 2C). Second, we tested a sequential IP strategy whereby magnetic beads conjugated to only one antibody were used for IP, and the resulting supernatant was used for a second IP with the other antibody. Each IP fraction was tested for the presence of RPL22-HA or RPL22-V5 by Western blot (Figure 2D). RPL22-HA and RPL22-V5 were only detected in IP fractions using HA or V5 antibodies, respectively, regardless of the order in which the IPs were performed. Thus, sequential IP can be used to separate epitope-tagged RPL22 from distinct cell populations.



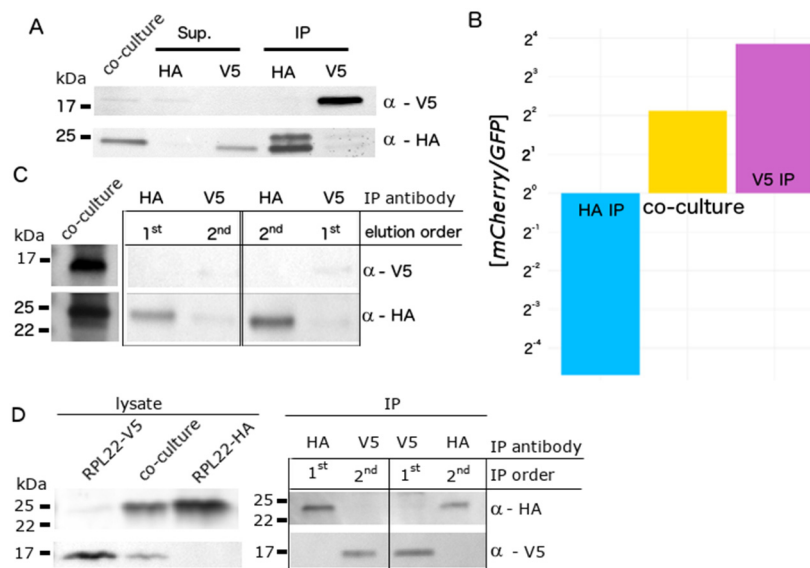


**Figure 2.** Co-culture of HEK293 cells expressing RPL22-HA or RPL22-V5. **(A)** Lysates, supernatants (Sup), and immunoprecipitated (IP) protein were resolved by SDS-PAGE, transferred to nitrocellulose, and probed with antibodies to HA or V5. **(B)** mCherry and GFP mRNA concentration was measured by reverse transcription digital PCR in RNA isolated from the co-culture (yellow), HA (blue), and V5 IP (purple), and plotted as a ratio. **(C)** RPL22-V5 and RPL22-HA were simultaneously IPed from co-culture lysates and selectively eluted in the indicated order using V5 or HA peptides, respectively. Co-culture lysates and IPed protein were resolved by SDS-PAGE, transferred to nitrocellulose, and probed with antibodies to V5 or HA. **(D)** RPL22-V5 and RPL22-HA were sequentially IPed in the indicated order from co-culture lysates. Lysates and IPed protein were resolved by SDS-PAGE, transferred to nitrocellulose, and probed with antibodies to HA or V5.

### 3.3. Transcriptome-Wide Cell Type-Specific Enrichment in Mixed Species Co-Cultures Using RiboTags

To assess cell type-specific enrichment transcriptome-wide, we co-cultured human (HEK293) and mouse (NIH-3T3) cells transduced with  $P_{TRE}$ -GFP-T2A-RPL22-HA and  $P_{TRE}$ -mCherry-T2A-RPL22-V5, respectively. IPs were carried out sequentially using both possible orders (e.g., HA then V5 and vice versa). We observed a greater than 1000-fold difference in the *mCherry/GFP* ratio, as measured by RT-dPCR, between the HA and V5 IP mRNA regardless of the order in which the IPs were performed (Figure 3A, Table S5). For both HA and V5 IPs, the RNA yield was reduced in the second IP (Table S6). We next used RNA-seq to evaluate transcriptome-wide cell type-specific mRNA enrichment (Figure 3B). Reads were assigned as human or mouse using STAR [49] by aligning all reads to a combined reference genome consisting of the canonical chromosomes from GRCh38 (human) and GRCm38 (mouse) and sequences for *GFP* and *mCherry*. *GFP* and *mCherry* read counts were consistent with RT-dPCR results (Figure S4, Table S7). The initial species composition of reads in the mixed co-culture was 72% mouse and 28% human (Figure 3B; Table S7). IP using HA or V5 antibodies increased the read composition of human and mouse reads, respectively, and the species composition was similar regardless of the order that the IPs were performed. As expected, gene expression from HEK293 monocultures correlated with HA IP samples whereas V5 IP samples more closely correlated with NIH 3T3 monocultures (Figure 3C).

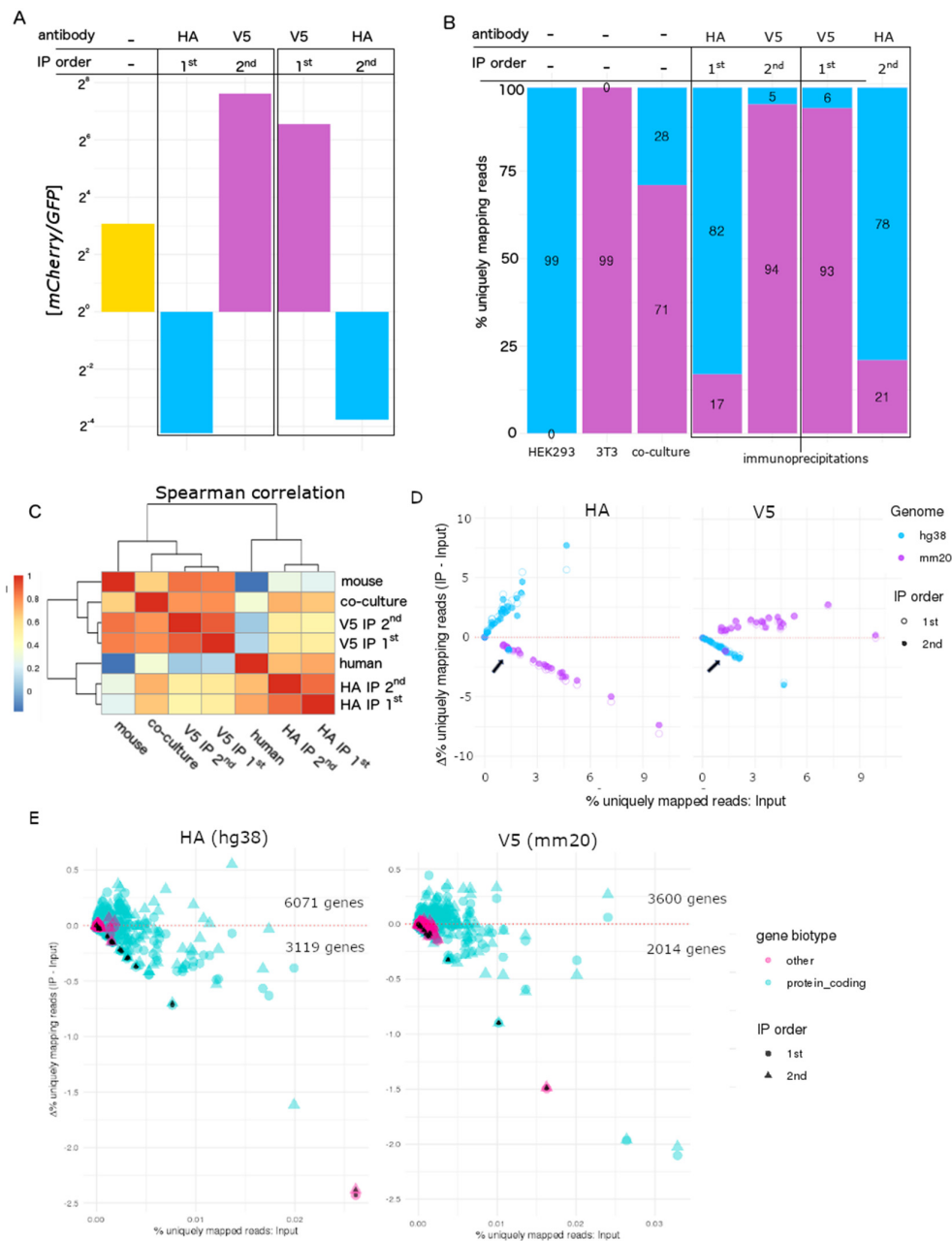


**Figure 3.** Application of RiboTags to mixed species co-cultures of HEK293 cells expressing RPL22-HA and NIH3T3 cells expressing RPL22-V5. **(A)** mCherry and GFP mRNA concentration was measured by reverse transcription digital PCR in RNA isolated from the co-culture (yellow), HA IP (blue), and V5 IP (purple), and plotted as a ratio. **(B)** RNA-seq reads were mapped to a hybrid reference genome containing hg38 and mm20 chromosomes and quantified by species for monocultures, co-culture, and IP samples. **(C)** Spearman correlation plot of RNA-seq for co-culture and IP samples. **(D)** The change in uniquely mapping reads (IP—input) for each chromosome was plotted against the initial (Input) percent uniquely mapping reads. Each dot represents a chromosome (hg38—blue, mm20—purple). First and second IPs are represented by open and filled dots, respectively. Chromosomes that fall above the red dotted line were enriched whereas chromosomes that fall below the red dotted line were depleted in IP samples compared to the Input. **(E)** The change in on target (e.g., hg38 for HA IP and mm20 for V5) percent uniquely mapping reads (IP—Input) was plotted against the initial (Input) percent uniquely mapping reads at the gene level. Protein coding genes are in cyan and non-protein coding genes in pink. First and second IPs are represented by circles and triangles, respectively. Mitochondrially encoded genes have additional black colored fill.

There was considerable cross-species contamination despite species-specific expression of HA or V5-tagged RPL22. For RNA isolated by HA IP, we considered reads that uniquely mapped to the human genome as on-target and uniquely mapped mouse reads as off-target; we inverted the analysis for V5 IPs. We quantified the number of reads mapping to each human and mouse chromosome before and after IP and plotted the change (e.g., input—IP) for each chromosome (Figure 3D). Except for the mitochondrial genome, (Figure 3D—arrows), which was not translated by RPL22-containing ribosomes, chromosomes with on-target reads were enriched and those with off-target reads were depleted. When RPL22-HA was expressed in HEK293 cells, HA IP resulted in enrichment of reads mapping to hg38 (Figure 3D—HA; blue dots above the *x*-axis). Similarly, when RPL22-V5 expression was restricted to NIH3T3 cells, V5 IP enriched reads mapping to mm20 chromosomes (Figure 3D—V5; purple dots above the *x*-axis). We observed a striking negative correlation for the depletion of off-target reads ( $R^2 = 0.99$ ; Table 1), the negative slope of which we define as the depletion efficiency (0.74–0.85; Table 1). The maximum theoretical depletion efficiency is 1 (see materials and methods). We performed a similar analysis for on-target reads at the gene level (Figure 3E). As expected, mitochondrially encoded genes were depleted in a manner similar to off-target genes in both cases (Figure 3E—black fill). The relative change (IP—input) varied considerably across on-target protein coding genes. More protein coding genes were enriched than depleted. Conversely, non-protein coding genes were primarily depleted.

**Table 1.** Relative enrichment of species-specific mRNA in mouse/human co-cultures using RiboTags. The change in uniquely mapping reads (IP—input) for each mouse and human chromosome was plotted against the initial (Input) percent uniquely mapping reads. Below is the species-specific linear regression of the change in uniquely mapping reads from (% unique reads vs.  $\Delta$  unique reads) at a chromosome level. ‘Species’ indicates which chromosomes were used to calculate the regression, and ‘off/on target’ indicates whether RPL22 was expressed in that species (on-target) or not (off-target).

Sample	IP Order	Species	On/Off Target	Slope	R <sup>2</sup>	p-Value
V5-1 (3T3)	1	human	off target	−0.8	0.99	$p < 0.001$
	1	mouse	on target	0.12	0.08	$p < 0.10$
V5-2 (3T3)	2	human	off target	−0.85	0.99	$p < 0.001$
	2	mouse	on target	0.14	0.12	$p < 0.06$
HA-1 (HEK293)	1	human	on target	1.26	0.59	$p < 0.001$
	1	mouse	off target	−0.81	0.99	$p < 0.001$
HA-2 (HEK293)	2	human	on target	1.56	0.74	$p < 0.001$
	2	mouse	off target	−0.74	0.99	$p < 0.001$

### 3.4. Application of RiboTag to hiPSC-Derived Neural Cell Types

The expanding repertoire of directed differentiation and neural induction protocols allows in vitro studies of a variety of human neural cells from donor-specific genetic backgrounds. We constructed stable hiPSC and neural progenitor cell (NPC) lines using lentiviral vectors encoding RiboTags. GFP or mCherry accumulation diminished over long-term culture in NPCs that constitutively express epitope-tagged RPL22. We also observed low and inconsistent P<sub>TRE</sub>-RiboTag expression in MNs derived from RiboTag-transduced hiPSCs that were purified by flow cytometry. Thus, long-term culture and differentiation may be associated with gene silencing. Lentiviral transduction of P<sub>TRE</sub>-RiboTags during neural induction or in differentiated neurons improved RiboTag expression. Marker gene expression was confirmed by RNA-seq (Figure 4A) for hiPSC-derived MNs (n = 7 input; n = 3 IP), GABAergic neurons (iGANs; n = 2 input; n = 2 IP), and NPCs (n = 1 input; n = 1 IP). We confirmed RPL22 immunoprecipitation by Western blot (Figure 4B). Using Ensembl gene biotypes to categorize annotated genes, we observed a significant enrichment of protein coding transcripts and a concomitant decrease in long non-coding RNA (lncRNA) and pseudogenes (Figure 4C). In contrast, mitochondrial protein coding transcripts were depleted in IP samples compared to input controls (Figure 4D). Thus, RiboTags can be expressed in hiPSC-derived cells and used to enrich translated mRNA by IP.

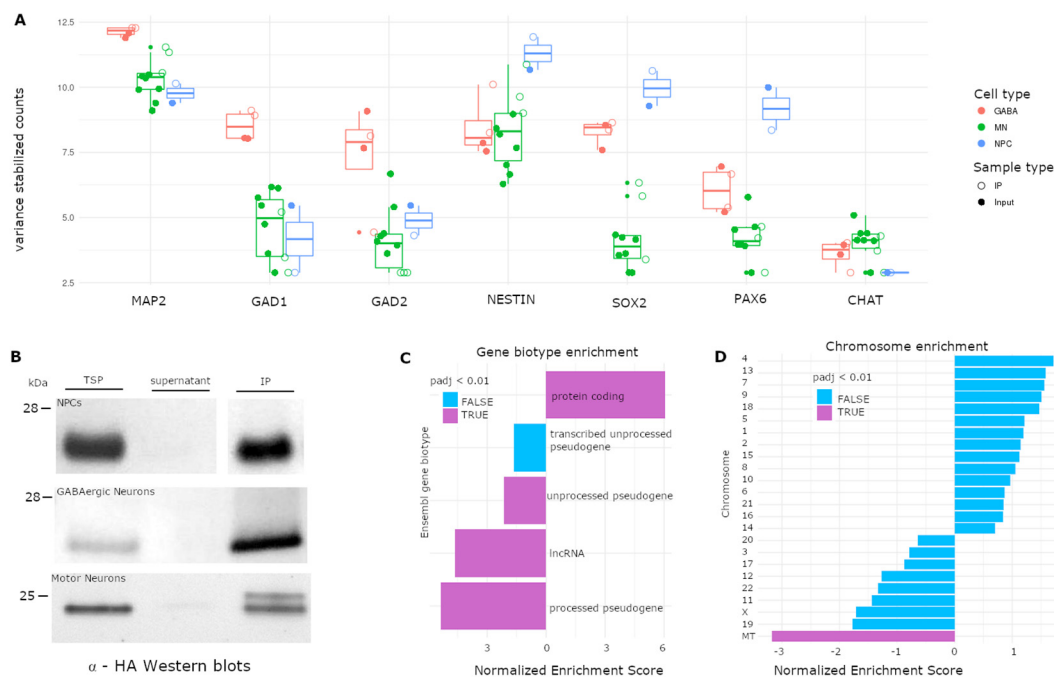


**Figure 4.** Application of RiboTags to hiPSC-derived neural progenitor cells (NPCs), GABAergic neurons (iGABAs), and motor neurons (MNs). **(A)** Variance stabilized counts of neural (MAP2), GABAergic (GAD1, GAD2), neural progenitor (NESTIN, SOX2, PAX6), and cholinergic (CHAT) marker genes from hiPSC-derived NPCs (blue), iGABAs (salmon), and MNs (green) from input (filled dots) and IP (open dots) samples using RNA-seq. **(B)** Total soluble protein (TSP), supernatants (Sup), and immunoprecipitated (IP) protein were resolved by SDS-PAGE, transferred to nitrocellulose, and probed with antibodies to HA for hiPSC-derived NPCs, iGABAs, and MNs. **(C)** Gene set enrichment analysis (GSEA) using Ensembl gene biotypes across all annotated genes. **(D)** GSEA of protein-coding genes grouped by chromosomes. P-values are adjusted for gene set size and the number of gene sets tested. Bars are colored by whether a gene set reached significance (Purple— $p < 0.01$ ; Blue— $p > 0.01$ ).

We next applied  $P_{TRE}$ -RiboTag to co-cultures of hiPSC-derived MNs (hiPSC-MNs) and primary mouse astrocytes. Cells were transduced with  $P_{TRE}$ -RiboTag (HA or V5) lentivirus as monocultures, mixed, and co-cultured for two weeks. We prepared six independent co-cultures ( $n = 5$  independent hiPSC-MN differentiations) using mixed species cocultures to evaluate the variability between experiments. For five of the six co-cultures, mAstros and hiPSC-MNs were transduced with RPL22-HA and RPL22-V5, respectively. The RiboTags were reversed for a single co-culture. RNA purified from co-cultures and matched hiPSC-MN ( $n = 6$ ) or mAstro ( $n = 3$ ) IPs was analyzed by RNA-seq. Reads were aligned to a hybrid reference before protein coding reads were quantified. Reporter gene expression was not significantly different between RiboTags or cell types (Figure S5A,B). The species composition of the RNA across independent co-cultures varied by as much as 50% (Figure 5A—yellow dots, Figure S5C). *GFP* or *mCherry* enrichment relative to co-cultures ranged from 2.4- to 194-fold (Figure S5D). As expected, the percentage of hg38-mapped reads increased (compared to matched co-cultures) when IPs were performed with antibodies against RiboTags expressed in hiPSC-MNs (Figure 5A; blue-V5, purple-HA). Conversely, the percentage of hg38-mapped reads decreased when IPs were performed with antibodies against RiboTags expressed in primary mouse astrocytes (Figure 5A; purple-HA). Similar to co-cultures using HEK293 and NIH3T3 cells, we observed an enrichment of reads mapping to on-target chromosomes and depletion of reads mapping to off-target chromosomes compared to the co-culture (Figure S6). Depletion efficiency ranged from 0.25–0.84 and 0.46–0.87 for RPL22-V5 and RPL22-HA, respectively (Figure 5B). The correlation between the percentage of reads mapping to off-target chromosomes in co-culture vs. IP samples was reduced for low-efficiency IPs (Figure 5B, Figure S6, Table 2). Reporter gene expression (*GFP/mCherry*), which is a proxy for

RiboTag expression, and initial co-culture composition did not correlate with depletion efficiency (Figure S7). Thus, differential RiboTag expression in mixed co-cultures allowed for cell type-specific RNA enrichment, but the enrichment was not consistent across replicates.

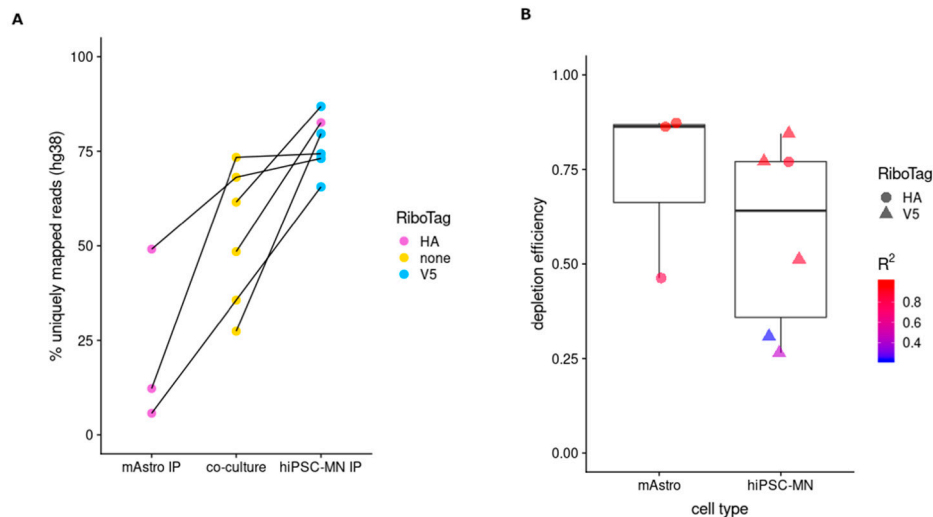


**Figure 5.** Application of RiboTags to co-cultures of hiPSC-derived motor neurons and primary mouse astrocytes. Six independent hiPSC-MNs/mAstros co-cultures were used to evaluate the variability between replicates. RNA-seq reads were mapped to an hg38/mm20 hybrid reference genome, and reads that mapped to protein coding genes were quantified. **(A)** For each co-culture ( $n = 6$ ) and IP ( $n = 3$  for mAstro;  $n = 6$  for hiPSC-MN), the percentage of reads that mapped to hg38 was plotted (the percentage of reads mapped to mm20 is equal to the plotted value subtracted from 100). The on-target cell type for each IP is indicated on the  $x$ -axis, and the RiboTag used to transduce the on-target cell type is indicated by color (purple—RPL22-HA; blue—RPL22-V5). For example, a purple dot above mAstro corresponds to the percentage of reads mapped to hg38 in RNA isolated from a co-culture wherein RPL22-HA was expressed in mAstros and anti-HA antibodies were used for the IP. Lines connecting colored dots indicate matched samples (e.g., IPs came from the indicated co-culture). **(B)** The depletion efficiency was calculated for HA (circles) and V5 (triangles) RiboTag samples using off-target reads (mm20 for hiPSC-MN IPs; hg38 for mAstro IPs). Color indicates the R-squared value for the linear regression between the IP sample and the matched co-culture.

**Table 2.** Relative depletion of off-target mRNA in co-cultures of hiPSC-motor neurons and primary mouse astrocytes. The change in uniquely mapping reads (IP—input) for each mouse and human chromosome was plotted against the initial (Input) percent uniquely mapping reads. Below is the species-specific linear regression of the change in uniquely mapping reads from (% unique reads vs.  $\Delta$  unique reads) at a chromosome level for the off-target species (e.g., only relative depletion is shown).

Library	Input Library	MN Differentiation	IP Cell Type	RiboTag	Species	Slope	R Squared	$p$ Value	RNA Yield (ng)
5	2	20190603	mAstro	HA	mouse	-0.46	0.82	0.001	593.6
8	2	20190603	MN	V5	human	-0.26	0.42	0.001	<1
12	10	20190528	mAstro	HA	mouse	-0.87	0.99	0.001	158.2
14	10	20190528	MN	V5	human	-0.31	0.23	0.017	422.8
20	17	20190417	mAstro	HA	mouse	-0.86	0.99	0.001	431.2
18	17	20190417	MN	V5	human	-0.51	0.91	0.001	<1
28	21	20190610	MN	V5	human	-0.77	0.96	0.001	187.6
30	23	20190610	MN	HA	human	-0.77	0.94	0.001	<1
31	25	20190617	MN	V5	human	-0.84	0.96	0.001	<1



#### 4. Discussion

Our report demonstrates that restricting the expression of uniquely-tagged RPL22 (RiboTags) to specific cell types within a mixed co-culture allows for enrichment of cell type-specific translomes. We fused three commonly used epitope tags (hemagglutinin—HA, V5, and Flag) to the C-terminus of RPL22 and found that V5 and HA, but not Flag RiboTags, facilitated immunoprecipitation of RNA via RNA-bound ribosomes. The failure of RPL22-Flag IP to capture RNA is likely due to inefficient incorporation into the ribosome as indicated by the failure to co-IP RPLP0. Using mixed species co-cultures, we demonstrated that RiboTags can be sequentially IPed without detectable cross contamination by Western blot. Despite efficient separation of the RiboTag protein, we observed cross contamination of RNA in RiboTag IPs from mixed species co-cultures. The efficiency of off-target RNA depletion (~80%) was consistent between HA and V5 RiboTags.

We encountered several challenges when applying RiboTags to hiPSCs and hiPSC-derived neural cells. First, constitutive RiboTag expression with the Ef1-alpha promoter was associated with gene silencing in replicative cells (e.g., hiPSCs, NPCs, HEK293s) and reduced viability in post-mitotic cells (e.g., hiPSC-derived neurons). We found that inducible RiboTag expression using the tetracycline response element (TRE) circumvented both of these issues. Approximately twenty-four hours of doxycycline treatment was sufficient for all cell types tested. Reducing the duration or magnitude of induction could minimize potential adverse effects. Promoters with 'weaker' activity could also be explored. Second, doxycycline-dependent RiboTag expression was robust in stably transduced hiPSC lines isolated by FACS. However, motor neurons derived from these lines exhibited low and inconsistent expression after the addition of doxycycline. Thus, directed neuronal differentiation may also be associated with gene silencing. RiboTag expression was more robust when neural cells were transduced post dual-SMAD inhibition (see materials and methods). Third, transcription factor overexpression protocols for neural induction frequently use TRE because it is reliable and plasmids are readily available. Although not tested here, we constructed HA and V5 RiboTag vectors flanked by double-floxed inverse orientation (DIO) sequences (Figure S8) that are compatible with TRE. These vectors could be used in combination with a tamoxifen-inducible Cre or with Cre driven by a cell type-specific promoter [53]. Lastly, cell proportions are difficult to control over long-term culture because astrocytes are proliferative and neurons are post-mitotic.

The challenges outlined above likely contribute to the variability in the depletion efficiency of off-target mRNA. Consistent with differentiation and transduction contributing to technical variability, we observed more consistent reporter gene ratios (mCherry/GFP) across replicates from co-cultures prepared from a single differentiation and transduction per cell type (Figure S9). However, we cannot rule out that the depletion efficiency may be inherently more variable across hiPSC donors, cell types, or differentiation protocols. Knocking in RiboTags at the native RPL22 locus could reduce variability due to differences in expression and could eliminate the need for lentiviral transductions. Such labor-intensive and time-consuming strategies would have to be weighed against the need to include multiple donor hiPSC lines, which is more easily accomplished using lentiviral expression.

RiboTag based enrichment did not eliminate all off-target RNA in hiPSC-derived neurons or primary mouse astrocytes. This may be due to non-specific antibody-RNA interactions or RiboTag-containing ribosomes that bind off-target RNA after cell lysis. Importantly, these technical challenges may be relevant for *in vivo* experiments also, but unlike in this study, contaminating RNA cannot be empirically measured using mixed species co-cultures. Improved purification protocols would need to be compatible across epitope-tags. Whether similar levels of contaminating RNA are observed using RPL10a instead of RPL22 needs to be investigated. Careful consideration should be taken to evaluate the level of contaminating RNA and the relative proportion of cells to better inform the downstream analysis. Here, we used mixed species experiments to empirically determine the depletion efficiency using off-target RNA. Mitochondrial genes could be used in a similar manner, but would overestimate the depletion efficiency in same-species co-cultures because both cell types express the same mitochondrial genes. We also used uniquely expressed reporter genes, but these

provide only a single datapoint. Computational approaches similar to those used to deconvolve cell type-specific signatures from bulk tissue could be implemented, particularly if information about depletion efficiency is incorporated.

RiboTag and TRAP methods are widely used to investigate cell type-specific transcriptomes in vivo. We anticipate that as in vitro cultures become increasingly complex in an attempt to more closely mimic in vivo cellular networks, methods that disambiguate cell type-specific transcriptomes and avoid the complexity and expense of scRNA-seq methods will be necessary. For example, RiboTags could be used to capture cell type-specific RNA from organoids (Figure S10) and could conceivably be used to capture RNA from multiple cell types simultaneously. scRNA-seq can generate cell type-specific transcriptomes by virtue of profiling thousands of single cells at once. Specific cell types can also be enriched prior to scRNA-seq using FACS-based methods. While the cost and scale of scRNA-seq are rapidly improving, it remains cost-prohibitive for large-scale studies and limited to the most abundant transcripts. RiboTag and TRAP are complementary to scRNA-seq and could even be used in parallel to deeply interrogate full-length transcripts, yielding information about low-abundant transcripts and splicing that are missed by scRNA-seq. Together, these methods are promising avenues for dissecting cell type-specific gene expression in complex in vitro cultures.

**Supplementary Materials:** The following are available online at <http://www.mdpi.com/2073-4409/9/6/1406/s1>. Figure S1: Diagram of RiboTag lentiviral constructs. Figure S2: Diagram of inducible RiboTag lentiviral constructs. Figure S3: Co-cultures of HEK293 cells transduced with V5 and HA RiboTag vectors. Figure S4: Reverse transcription digital PCR (RT-dPCR) of *mCherry* and *GFP* from co-cultured human (HEK293) and mouse (NIH-3T3) cells transduced with  $P_{TRE}$ -GFP-T2A-RPL22-HA and  $P_{TRE}$ -mCherry-T2A-RPL22-V5, respectively. Figure S5: RiboTag expression and cell-type specific enrichment in hiPSC-MN and primary mouse astrocyte co-cultures. Figure S6: Relative enrichment of human and mouse RNA in RiboTag IPs compared to co-cultures of hiPSC-MNs and primary mouse astrocytes. Figure S7: Correlation of RiboTag expression and the initial coculture species composition with depletion efficiency of RiboTag IPs. Figure S8: Diagram of double-floxed inverse orientation (DIO) lentiviral RiboTag constructs. Figure S9: Reverse transcription digital PCR (RT-dPCR) of *mCherry* and *GFP* from RiboTag co-cultures. Figure S10: Reverse transcription digital PCR (RT-dPCR) of *GFP* and *MTCO2* from HMC3 microglia expressing GFP-T2A-RPL22-HA co-cultured with neurospheres. Table S1: List of primers/probes. Table S2: List of plasmids. Table S3: Raw digital PCR data from HEK293 mixed culture (RPL22-HA-GFP or RPL22-V5-mCherry). Table S4: Reporter gene ratios in HEK293 mixed experiment (RPL22-HA-GFP or RPL22-V5-mCherry) using digital PCR. Table S5: Raw digital PCR data from mixed species co-culture (HEK293/RPL22-HA-GFP; NIH3T3/RPL22-V5-mCherry). Table S6: RNA yields for NIH3T3/HEK293 immunoprecipitations. Table S7: Counts tabulated using samtools from NIH3T3/HEK293 RNA-seq aligned to a hybrid reference genome.

**Author Contributions:** Conceptualization, J.A.G., K.J.B., H.P. and J.A.G. Data curation, J.A.G., E.H. Formal analysis, J.A.G., E.H. Funding acquisition, J.A.G., H.P. Investigation, J.A.G., G.A., E.H., C.B., M.C., M.H., N.B., R.A., K.K. Resources, S.T., C.M.K., A.G., E.C., K.B., S.L., and S.G. Methodology, J.A.G. Software, J.A.G., N.S. Supervision, J.A.G., H.P. Visualization, J.A.G. Writing—original draft, J.A.G. Writing—review & editing, G.H., E.H., K.J.B., J.A.G. All authors have read and agreed to the published version of the manuscript.

**Funding:** This work was supported by Project ALS. ALS sequencing efforts at NYGC are supported by the ALS Association (Grant #19-SI-459) and the Tow Foundation. This work was partially supported by the National Institutes of Health (NIH) grants R56 MH101454 (K.J.B.), R01 MH106056 (K.J.B.), and R01 MH109897 (K.J.B.). We thank Neuracell core facility, NSCI, Rensselaer NY, for generating the organoids and the Tau Consortium and Rainwater Charitable Foundation for their support of organoid production.

**Acknowledgments:** We thank Thi Vo and Philip De Jager for the HMC3 cell line. We also thank Stan McKnight for the pAAV-Ef1a-DIO-eYFP plasmid.

**Conflicts of Interest:** The authors declare no conflict of interest.

## References

1. Van Horn, M.R.; Ruthazer, E.S. Glial regulation of synapse maturation and stabilization in the developing nervous system. *Curr. Opin. Neurobiol.* **2019**, *54*, 113–119. [[CrossRef](#)] [[PubMed](#)]
2. Sims, R.; van der Lee, S.J.; Naj, A.C.; Bellenguez, C.; Badarinarayan, N.; Jakobsdottir, J.; Kunkle, B.W.; Boland, A.; Raybould, R.; Bis, J.C.; et al. Rare coding variants in *PLCG2*, *ABI3*, and *TREM2* implicate microglial-mediated innate immunity in Alzheimer's disease. *Nat. Genet.* **2017**, *49*, 1373–1384. [[CrossRef](#)] [[PubMed](#)]

3. Gonzalez, D.M.; Gregory, J.; Brennand, K.J. The Importance of Non-neuronal Cell Types in hiPSC-Based Disease Modeling and Drug Screening. *Front Cell Dev. Biol.* **2017**, *5*, 117. [[CrossRef](#)] [[PubMed](#)]
4. Li, L.; Chao, J.; Shi, Y. Modeling neurological diseases using iPSC-derived neural cells: iPSC modeling of neurological diseases. *Cell Tissue Res.* **2018**, *371*, 143–151. [[CrossRef](#)] [[PubMed](#)]
5. Birey, F.; Andersen, J.; Makinson, C.D.; Islam, S.; Wei, W.; Huber, N.; Fan, H.C.; Metzler, K.R.C.; Panagiotakos, G.; Thom, N.; et al. Assembly of functionally integrated human forebrain spheroids. *Nature* **2017**, *545*, 54–59. [[CrossRef](#)] [[PubMed](#)]
6. Dezonne, R.S.; Sartore, R.C.; Nascimento, J.M.; Saia-Cereda, V.M.; Romão, L.F.; Alves-Leon, S.V.; de Souza, J.M.; Martins-de-Souza, D.; Rehen, S.K.; Gomes, F.C.A. Derivation of Functional Human Astrocytes from Cerebral Organoids. *Sci. Rep.* **2017**, *7*, 45091. [[CrossRef](#)]
7. Marton, R.M.; Miura, Y.; Sloan, S.A.; Li, Q.; Revah, O.; Levy, R.J.; Huguenard, J.R.; Paşca, S.P. Differentiation and maturation of oligodendrocytes in human three-dimensional neural cultures. *Nat. Neurosci.* **2019**, *22*, 484–491. [[CrossRef](#)]
8. Abud, E.M.; Ramirez, R.N.; Martinez, E.S.; Healy, L.M.; Nguyen, C.H.H.; Newman, S.A.; Yeromin, A.V.; Scarfone, V.M.; Marsh, S.E.; Fimbres, C.; et al. iPSC-Derived Human Microglia-like Cells to Study Neurological Diseases. *Neuron* **2017**, *94*, 278–293.e9. [[CrossRef](#)]
9. Cakir, B.; Xiang, Y.; Tanaka, Y.; Kural, M.H.; Parent, M.; Kang, Y.-J.; Chapeton, K.; Patterson, B.; Yuan, Y.; He, C.-S.; et al. Engineering of human brain organoids with a functional vascular-like system. *Nat. Methods* **2019**, *16*, 1169–1175. [[CrossRef](#)]
10. Vatine, G.D.; Barrile, R.; Workman, M.J.; Sances, S.; Barriga, B.K.; Rahnama, M.; Barthakur, S.; Kasendra, M.; Lucchesi, C.; Kerns, J.; et al. Human iPSC-Derived Blood-Brain Barrier Chips Enable Disease Modeling and Personalized Medicine Applications. *Cell Stem Cell* **2019**, *24*, 995–1005.e6. [[CrossRef](#)]
11. Lobo, M.K.; Karsten, S.L.; Gray, M.; Geschwind, D.H.; Yang, X.W. FACS-array profiling of striatal projection neuron subtypes in juvenile and adult mouse brains. *Nat. Neurosci.* **2006**, *9*, 443–452. [[CrossRef](#)] [[PubMed](#)]
12. Arlotta, P.; Molyneaux, B.J.; Chen, J.; Inoue, J.; Kominami, R.; Macklis, J.D. Neuronal subtype-specific genes that control corticospinal motor neuron development in vivo. *Neuron* **2005**, *45*, 207–221. [[CrossRef](#)] [[PubMed](#)]
13. Ramsköld, D.; Luo, S.; Wang, Y.-C.; Li, R.; Deng, Q.; Faridani, O.R.; Daniels, G.A.; Khrebtkova, I.; Loring, J.F.; Laurent, L.C.; et al. Full-length mRNA-Seq from single-cell levels of RNA and individual circulating tumor cells. *Nat. Biotechnol.* **2012**, *30*, 777–782. [[CrossRef](#)] [[PubMed](#)]
14. Tang, F.; Barbacioru, C.; Wang, Y.; Nordman, E.; Lee, C.; Xu, N.; Wang, X.; Bodeau, J.; Tuch, B.B.; Siddiqui, A.; et al. mRNA-Seq whole-transcriptome analysis of a single cell. *Nat. Methods* **2009**, *6*, 377–382. [[CrossRef](#)] [[PubMed](#)]
15. Bonner, R.F.; Emmert-Buck, M.; Cole, K.; Pohida, T.; Chuaqui, R.; Goldstein, S.; Liotta, L.A. Laser capture microdissection: Molecular analysis of tissue. *Science* **1997**, *278*, 1481–1483. [[CrossRef](#)] [[PubMed](#)]
16. Emmert-Buck, M.R.; Bonner, R.F.; Smith, P.D.; Chuaqui, R.F.; Zhuang, Z.; Goldstein, S.R.; Weiss, R.A.; Liotta, L.A. Laser capture microdissection. *Science* **1996**, *274*, 998–1001. [[CrossRef](#)] [[PubMed](#)]
17. Rossner, M.J.; Hirrlinger, J.; Wichert, S.P.; Boehm, C.; Newrzella, D.; Hiemisch, H.; Eisenhardt, G.; Stuenkel, C.; von Ahnen, O.; Nave, K.-A. Global transcriptome analysis of genetically identified neurons in the adult cortex. *J. Neurosci.* **2006**, *26*, 9956–9966. [[CrossRef](#)]
18. Stoeckius, M.; Hafemeister, C.; Stephenson, W.; Houck-Loomis, B.; Chattopadhyay, P.K.; Swerdlow, H.; Satija, R.; Smibert, P. Simultaneous epitope and transcriptome measurement in single cells. *Nat. Methods* **2017**, *14*, 865–868. [[CrossRef](#)]
19. Mimitou, E.P.; Cheng, A.; Montalbano, A.; Hao, S.; Stoeckius, M.; Legut, M.; Roush, T.; Herrera, A.; Papalexi, E.; Ouyang, Z.; et al. Multiplexed detection of proteins, transcriptomes, clonotypes and CRISPR perturbations in single cells. *Nat. Methods* **2019**, *16*, 409–412. [[CrossRef](#)]
20. Coenen, C.; Liedtke, S.; Kogler, G. RNA Amplification Protocol Leads to Biased Polymerase Chain Reaction Results Especially for Low-Copy Transcripts of Human Bone Marrow-Derived Stromal Cells. *PLoS ONE* **2015**, *10*, e0141070. [[CrossRef](#)]
21. Okaty, B.W.; Sugino, K.; Nelson, S.B. Cell type-specific transcriptomics in the brain. *J. Neurosci.* **2011**, *31*, 6939–6943. [[CrossRef](#)] [[PubMed](#)]
22. Cobos, F.A.; Vandesompele, J.; Mestdagh, P.; De Preter, K. Computational deconvolution of transcriptomics data from mixed cell populations. *Bioinformatics* **2018**, *34*, 1969–1979. [[CrossRef](#)] [[PubMed](#)]

23. Sturm, G.; Finotello, F.; Petitprez, F.; Zhang, J.D.; Baumbach, J.; Fridman, W.H.; List, M.; Aneichyk, T. Comprehensive evaluation of transcriptome-based cell-type quantification methods for immuno-oncology. *Bioinformatics* **2019**, *35*, i436–i445. [[CrossRef](#)] [[PubMed](#)]
24. Sanz, E.; Yang, L.; Su, T.; Morris, D.R.; McKnight, G.S.; Amieux, P.S. Cell-type-specific isolation of ribosome-associated mRNA from complex tissues. *Proc. Natl. Acad. Sci. USA* **2009**, *106*, 13939–13944. [[CrossRef](#)]
25. Doyle, J.P.; Dougherty, J.D.; Heiman, M.; Schmidt, E.F.; Stevens, T.R.; Ma, G.; Bupp, S.; Shrestha, P.; Shah, R.D.; Doughty, M.L.; et al. Application of a translational profiling approach for the comparative analysis of CNS cell types. *Cell* **2008**, *135*, 749–762. [[CrossRef](#)]
26. Heiman, M.; Schaefer, A.; Gong, S.; Peterson, J.D.; Day, M.; Ramsey, K.E.; Suárez-Fariñas, M.; Schwarz, C.; Stephan, D.A.; Surmeier, D.J.; et al. A translational profiling approach for the molecular characterization of CNS cell types. *Cell* **2008**, *135*, 738–748. [[CrossRef](#)]
27. Nguyen, T.-M.; Schreiner, D.; Xiao, L.; Traunmüller, L.; Bornmann, C.; Scheiffele, P. An alternative splicing switch shapes neurexin repertoires in principal neurons versus interneurons in the mouse hippocampus. *Elife* **2016**, *5*, e22757. [[CrossRef](#)]
28. Brichta, L.; Shin, W.; Jackson-Lewis, V.; Blesa, J.; Yap, E.-L.; Walker, Z.; Zhang, J.; Roussarie, J.-P.; Alvarez, M.J.; Califano, A.; et al. Identification of neurodegenerative factors using translational regulatory network analysis. *Nat. Neurosci.* **2015**, *18*, 1325–1333. [[CrossRef](#)]
29. Haimon, Z.; Volaski, A.; Orthgiess, J.; Boura-Halfon, S.; Varol, D.; Shemer, A.; Yona, S.; Zuckerman, B.; David, E.; Chappell-Maor, L.; et al. Re-evaluating microglia expression profiles using RiboTag and cell isolation strategies. *Nat. Immunol.* **2018**, *19*, 636–644. [[CrossRef](#)]
30. Michalovicz, L.T.; Kelly, K.A.; Vashishtha, S.; Ben-Hamo, R.; Efroni, S.; Miller, J.V.; Locker, A.R.; Sullivan, K.; Broderick, G.; Miller, D.B.; et al. Astrocyte-specific transcriptome analysis using the ALDH1L1 bacTRAP mouse reveals novel biomarkers of astrogliosis in response to neurotoxicity. *J. Neurochem.* **2019**, *150*, 420–440. [[CrossRef](#)]
31. Zhu, Y.; Lyapichev, K.; Lee, D.H.; Motti, D.; Ferraro, N.M.; Zhang, Y.; Yahn, S.; Soderblom, C.; Zha, J.; Bethea, J.R.; et al. Macrophage Transcriptional Profile Identifies Lipid Catabolic Pathways That Can Be Therapeutically Targeted after Spinal Cord Injury. *J. Neurosci.* **2017**, *37*, 2362–2376. [[CrossRef](#)] [[PubMed](#)]
32. Southern, J.A.; Young, D.F.; Heaney, F.; Baumgärtner, W.K.; Randall, R.E. Identification of an epitope on the P and V proteins of simian virus 5 that distinguishes between two isolates with different biological characteristics. *J. Gen. Virol.* **1991**, *72*, 1551–1557. [[CrossRef](#)] [[PubMed](#)]
33. Field, J.; Nikawa, J.; Broek, D.; MacDonald, B.; Rodgers, L.; Wilson, I.A.; Lerner, R.A.; Wigler, M. Purification of a RAS-responsive adenyl cyclase complex from *Saccharomyces cerevisiae* by use of an epitope addition method. *Mol. Cell. Biol.* **1988**, *8*, 2159–2165. [[CrossRef](#)] [[PubMed](#)]
34. Hopp, T.P.; Prickett, K.S.; Price, V.L.; Libby, R.T.; March, C.J.; Pat Cerretti, D.; Urdal, D.L.; Conlon, P.J. A Short Polypeptide Marker Sequence Useful for Recombinant Protein Identification and Purification. *Biotechnology* **1988**, *6*, 1204–1210. [[CrossRef](#)]
35. Topol, A.; Zhu, S.; Hartley, B.J.; English, J.; Hauberg, M.E.; Tran, N.; Rittenhouse, C.A.; Simone, A.; Ruderfer, D.M.; Johnson, J.; et al. Dysregulation of miRNA-9 in a Subset of Schizophrenia Patient-Derived Neural Progenitor Cells. *Cell Rep.* **2017**, *20*, 2525. [[CrossRef](#)]
36. Lee, I.S.; Carvalho, C.M.B.; Douvaras, P.; Ho, S.-M.; Hartley, B.J.; Zuccherato, L.W.; Ladran, I.G.; Siegel, A.J.; McCarthy, S.; Malhotra, D.; et al. Characterization of molecular and cellular phenotypes associated with a heterozygous CNTNAP2 deletion using patient-derived hiPSC neural cells. *NPJ Schizophr.* **2015**, *1*, 15019. [[CrossRef](#)]
37. Ho, S.-M.; Hartley, B.J.; Tcw, J.; Beaumont, M.; Stafford, K.; Slesinger, P.A.; Brennand, K.J. Rapid Ngn2-induction of excitatory neurons from hiPSC-derived neural progenitor cells. *Methods* **2016**, *101*, 113–124. [[CrossRef](#)]
38. Tiscornia, G.; Singer, O.; Verma, I.M. Production and purification of lentiviral vectors. *Nat. Protoc.* **2006**, *1*, 241–245. [[CrossRef](#)]
39. Maury, Y.; Côme, J.; Piskorowski, R.A.; Salah-Mohellibi, N.; Chevaleyre, V.; Peschanski, M.; Martinat, C.; Nedelec, S. Combinatorial analysis of developmental cues efficiently converts human pluripotent stem cells into multiple neuronal subtypes. *Nat. Biotechnol.* **2015**, *33*, 89–96. [[CrossRef](#)]



40. Chambers, S.M.; Fasano, C.A.; Papapetrou, E.P.; Tomishima, M.; Sadelain, M.; Studer, L. Highly efficient neural conversion of human ES and iPS cells by dual inhibition of SMAD signaling. *Nat. Biotechnol.* **2009**, *27*, 275–280. [[CrossRef](#)]
41. O'Doherty, U.; Swiggard, W.J.; Malim, M.H. Human immunodeficiency virus type 1 spinoculation enhances infection through virus binding. *J. Virol.* **2000**, *74*, 10074–10080. [[CrossRef](#)] [[PubMed](#)]
42. Yang, N.; Chanda, S.; Marro, S.; Ng, Y.-H.; Janas, J.A.; Haag, D.; Ang, C.E.; Tang, Y.; Flores, Q.; Mall, M.; et al. Generation of pure GABAergic neurons by transcription factor programming. *Nat. Methods* **2017**, *14*, 621–628. [[CrossRef](#)] [[PubMed](#)]
43. Barretto, N.; Zhang, H.; Powell, S.K.; Fernando, M.B.; Zhang, S.; Flaherty, E.K.; Ho, S.-M.; Slesinger, P.A.; Duan, J.; Brennand, K.J. ASCL1- and DLX2-induced GABAergic neurons from hiPSC-derived NPCs. *J. Neurosci. Methods* **2020**, *334*, 108548. [[CrossRef](#)] [[PubMed](#)]
44. Harder, J.M.; Braine, C.E.; Williams, P.A.; Zhu, X.; MacNicoll, K.H.; Sousa, G.L.; Buchanan, R.A.; Smith, R.S.; Libby, R.T.; Howell, G.R.; et al. Early immune responses are independent of RGC dysfunction in glaucoma with complement component C3 being protective. *Proc. Natl. Acad. Sci. USA* **2017**, *114*, E3839–E3848. [[CrossRef](#)] [[PubMed](#)]
45. Yoon, S.-J.; Elahi, L.S.; Paşca, A.M.; Marton, R.M.; Gordon, A.; Revah, O.; Miura, Y.; Walczak, E.M.; Holdgate, G.M.; Fan, H.C.; et al. Reliability of human cortical organoid generation. *Nat. Methods* **2019**, *16*, 75–78. [[CrossRef](#)] [[PubMed](#)]
46. Karch, C.M.; Kao, A.W.; Karydas, A.; Onanuga, K.; Martinez, R.; Argouarch, A.; Wang, C.; Huang, C.; Sohn, P.D.; Bowles, K.R.; et al. A Comprehensive Resource for Induced Pluripotent Stem Cells from Patients with Primary Tauopathies. *Stem Cell Rep.* **2019**, *13*, 939–955. [[CrossRef](#)]
47. Obrig, T.G.; Culp, W.J.; McKeegan, W.L.; Hardesty, B. The mechanism by which cycloheximide and related glutarimide antibiotics inhibit peptide synthesis on reticulocyte ribosomes. *J. Biol. Chem.* **1971**, *246*, 174–181.
48. Krueger, F. Trim Galore: A Wrapper Tool around Cutadapt and FastQC to Consistently Apply Quality and Adapter Trimming to FastQ Files, With Some Extra Functionality for MspI-digested RRBS-type (Reduced Representation Bisulfite-Seq) Libraries. 2012. Available online: [http://www.Bioinformatics.Babraham.AC.UK/projects/trim\\_galore/](http://www.Bioinformatics.Babraham.AC.UK/projects/trim_galore/) (accessed on 28 April 2016).
49. Dobin, A.; Davis, C.A.; Schlesinger, F.; Drenkow, J.; Zaleski, C.; Jha, S.; Batut, P.; Chaisson, M.; Gingeras, T. STAR: Ultrafast universal RNA-seq aligner. *Bioinformatics* **2013**, *29*, 15–21. [[CrossRef](#)]
50. Liao, Y.; Smyth, G.K.; Shi, W. The Subread aligner: Fast, accurate and scalable read mapping by seed-and-vote. *Nucleic Acids Res.* **2013**, *41*, e108. [[CrossRef](#)]
51. Love, M.I.; Huber, W.; Anders, S. Moderated estimation of fold change and dispersion for RNA-seq data with DESeq2. *Genome Biol.* **2014**, *15*, 550. [[CrossRef](#)]
52. Korotkevich, G.; Sukhov, V.; Sergushichev, A. Fast gene set enrichment analysis. *bioRxiv* **2019**, 060012. [[CrossRef](#)]
53. Lesiak, A.J.; Brodsky, M.; Neumaier, J.F. RiboTag is a flexible tool for measuring the translational state of targeted cells in heterogeneous cell cultures. *Biotechniques* **2015**, *58*, 308–317. [[CrossRef](#)] [[PubMed](#)]

